Identification of protoneutron star g-modes in gravitational-wave data

I. INTRODUCTION

The life of massive stars ($8\mathrm{M}_\odot - 100\mathrm{M}_\odot$) ends with the collapse of their iron core under their own gravity, leading the formation of a neutron star or a black hole (BH), followed (typically but not necessarily in the BH case) by the explosion of the star as a supernova. Core-collapse supernova (CCSN) explosions are one of the expected sources of gravitational-waves (GW) that have not yet been detected by current ground-based observatories. This is because even the most common type of CCSN, the neutrino-driven explosion, have a rate about three per century [1] within our galaxy. The other main type of explosion, the magneto-rotational mechanism, can produce a more powerful signal and can be detected at distances up to ~ 5 Mpc [1] Add better reference. However, the rate of events of this kind is much lower than the one for the neutrino driven mechanism $\sim 10^{-4}\mathrm{yr}^{-1}$, which represents less than 1% of all CCSNe. Despite all this, collapsing stars produces a complex GW signal which could provide significant clues about the physical processes that occur in the moments after the collapse.

In the past years impressive progresses have been made in the development of numerical codes, which allow to obtain more accurate CCSN simulations. The waveforms produced by the magneto-rotational mechanism in particular is well understood. The core-bounce signal can be directly related with the rotational properties of the core [2–4]. However, the low rate of this kind of events and its expected low amplitude in the slow-rotation case, will probably impede its detection.

In the case of the neutrino-driven explosion mechanism, the GW emission is mainly produced during the hydrodynamical bounce and the unstable evolution of the fluid inside the region formed by the recently formed proto-neutron star (PNS) and the accretion shock. The dynamics excite the different modes of oscillation of the PNS [5, 6]. Unluckily, in this case it is not posible to relate the GW emission with the properties (mass, rotation rate, metallicity or magnetic fields) of the progenitor stars. A large number of physical processes are involved and their role is not completely understood. For instance, uncertainties in the stellar evolution models of massive stars or in the nuclear and weak interactions necessary for the equation of state (EoS) of nuclear matter or the neutrino interactions. Furthermore, the stochastic and chaotic nature of the instabilities is transferred to the GW emission, resulting in the same progenitor leading significantly different waveforms. The large number of physical ingredients in addition to the necessary accuracy of the modelling of complex multidimensional interactions requires large computational resources. One simulation of a single progenitor explosion in 3D with accurate neutrino transport and realistic EoS can take several months of intense calculations on a scientific supercomputer facility. This complicates the systematic exploration of the progenitor parameters.

Common features in the GW signal, that have been interpreted as gravity modes (g-modes) oscillations of the PNS, have been reported in many articles [7–12]. Typically, the frequencies associated with the modes rise monotonically with time during the contraction of the PNS. The characteristic frequencies of the modes associated to the PNS make them promising features for detection in ground-based interferometers. The presence of g-modes in hot PNS has been studied since the end of last century. The oscillation modes related with the surface of hot PNS was first considered by McDermott, van Horn & Scholl [13]. Additionally, the stratified structure of the PNS allows the presence of different types of g-modes related with the fluid core [14]. Many posterior works used simplified neutron star models assuming equilibrium configurations, to study the effect of rotation [15], general relativity [16], non-linearities [17], phase transition [18] and realistic equation of state [19]. Sotani & Takiwaki [20] studied the oscillation modes before the explosion using a simplified fits to numerical simulations.

In previous works [21, 22], we explore the eigenmode spectrum using results of CCSN numerical simulations and the theoretical model of the cavity form by the center of the PNS and the shock. We showed that the GW time-frequency distribution corresponds with the frequencies of oscillation of different families of p- and g-modes. These works reveal that is posible to perform CCSN asteroseismology and serves as a starting point to carry out inference of astrophysical parameters of PNSs. In this line of research, in [23] we derived the relations between the different types of modes with some with the evolution of mass and radius of the PNS. These relations are universal in the sense that they not depend of the EOS, the mass of the progenitor or the code used to perform the simulation.

In this paper, we present a method to extract from the GW data the mass and the radius of the PNS as function of time using the universal relations. We show how the algorithm is able to extract the time-frequency evolution of the main arc of GW emission, which corresponds to the ${}^2\mathrm{g}_2$ mode, according to the nomenclature used in [23]. The universal relation for this mode is inverted to obtain the time evolution of the ratio $r = M_{\mathrm{PNS}}/R_{\mathrm{PNS}}^2$. Using 2D CCSN waveform corresponding to different progenitor masses we estimate teh performance of the algorithm for current and future generation of ground-based GW detectors.

This paper is organised as follows. Section II describes the details of the 2D CCSN used. Section III focuses on the algorithm that extracts the time evolution of a combination of the mass and radius of the PNS corresponding to a g-mode. Section IV shows the performance of the data analysis method for different GW detectors. Finally, we discuss the results in section V.

II. CORE COLLAPSE SUPERNOVA SIMULATIONS

The algorithm proposed in the article does not require accurate waveforms but relies on the evolution of the frequencies of oscillations depending on the PNS mass and radius. To parametrize this dependence, we have considered spherically symmetric [22] and two-dimensional axisymmetric models of stellar core collapse simulated with two codes, CoCoNuT (one-dimensional models) and AENUS-ALCAR [24] (one- and two-dimensional models). CoCoNuT [25] is a code for general relativistic hydrodynamics coupled to the Fast Multigroup Transport scheme [26] providing an approximate description of the emission and transport of neutrinos. AENUS-ALCAR [24] combines special relativistic (magneto-)hydrodynamics, a modified Newtonian gravitational potential approximating the effects of general relativity [27], and a spectral two-moment neutrino transport solver [24]. We included the relevant reactions between matter and neutrinos of all flavours, i.e., emission and absorption by nucleons and nuclei, electron-positron pair annihilation, nucleonic bremsstrahlung, and scattering off nucleons, nuclei, and electrons.

We use two sets of 25 models in the range of initial stellar masses $M_{\rm ZAMS} = 11.2 - 75\,M_\odot$ simulated with the two codes. They were carried out using six equations of state (EOSs). In addition to these simulations data we have considered 8 waveforms. 7 of them are from two-dimensional axisymmetric models consisting of stellar core collapse of five stars with zero-age main-sequence masses of $M_{\rm ZAMS} = 11.2 - 40\,M_\odot$ evolved through the hydrostatic phases by [28]. We performed one simulation of each stellar model using the equation of state of [29] with an incompressibility of $K = 220\,\mathrm{MeV}$ (LS220) and added comparison simulations with the SFHo EOS [30] and the EOS of [31] (GShen) for the one with $M_{\rm ZAMS} = 15\,M_\odot$ (see Table I for a list of models). To this set of simulations, we add the waveform of a two-dimensional model used in [22], denoted `s20S`. It corresponds to a star with the same initial mass, $M_{\rm ZAMS} = 20\,M_\odot$, as for one of the other 7 axisymmetric simulations, but was taken from a newer set of stellar-evolution models [32]. It was evolved with the SFHo EOS.

We mapped the pre-collapse state of the stars to a spherical coordinate system with $n_r = 400$ zones in radial direction distributed logarithmically with a minimum grid width of $(\Delta r)_{\rm min} = 400\,\mathrm{m}$ and an outer radius of $r_{\rm max} = 8.3 \times 10^9\,\mathrm{cm}$ and $n_\theta = 128$ equidistant cells in angular direction. For the neutrino energies, we used a logarithmic grid with $n_e = 10$ bins up to $240\,\mathrm{MeV}$.

All spherical and most axisymmetric models fail to achieve shock revival during the time of our simulations. Only the two stars with the highest masses, `s25` and `s40`, develop relatively late explosions in axisymmetry. Consequently, mass accretion onto the PNSs proceeds at high rates for a long time in all cases and causes them to oscillate with their characteristic frequencies. The final masses of the PNSs are in the range of $M_{\rm PNS} = 1.47 - 2.33\,M_\odot$, i.e., insufficient for producing a black hole.

Simulation	$M_{\rm ZAMS}[M_\odot]$	EOS	$t_{\rm f}[\mathrm{s}]$	explosion	$M_{\rm PNS}[M_\odot]$
`s11`	11.2	LS220	1.86	$\times$	1.47
`s15`	15.0	LS220	1.66	$\times$	2.00
`s15S`	15.0	SFHo	1.75	$\times$	2.02
`s15G`	15.0	GShen	0.97	$\times$	1.86
`s20`	20.0	LS220	1.53	$\times$	1.75
`s20S`	20.0	SFHo	0.87	$\times$	2.05
`s25`	25.0	LS220	1.60	0.91	2.33
`s40`	40.0	LS220	1.70	1.52	2.23

TABLE I. List of axisymmetric simulations. We present the name of the models, the initial mass of the progenitors, and the EOS used, and the final post-bounce time of the simulations. For models which explode, we list the time at which the shock starts to expand in column "explosion"; otherwise, a $\times$ sign is displayed. The final column indicates the mass of the PNS at the end of the simulation.

III. METHODS DESCRIPTION

In this section, we outline a strategy for estimating the time evolution of the ratio $r = M_{\rm PNS}/R_{\rm PNS}^2$ of the mass of the PNS and its squared radius (in units of solar mass and km) from the observation of the ${}^2g_2$ oscillation mode in the gravitational wave detector data. An integral part of this strategy is the universal relations that relate the characteristic frequency of the PNS oscillation f, g and p modes with the mass and the radius of the PNS, the shock radius and the total mass inside the shock as demonstrated in [23].

Using 25 spherically symetric (1D) simulations obtained with the AENUS-ALCAR code [24] and the CoCoNuT [25] code, we parametrize the ratio with a cubic polynomial regression with heteroscedastic errors

$$r_i = \beta_1 f_i + \beta_2 f_i^2 + \beta_3 f_i^3 + \epsilon_i \tag{1}$$

where ϵ_i are assumed to be independent zero-mean Gaussian errors with variances σ_i^2 that increase with frequency f_i. The model for frequency-dependent variances is

$$\log \sigma_i = \alpha_0 + \alpha_1 f_i + \alpha_2 f_i^2 + \delta_i \tag{2}$$

with independent and identically zero-mean Gaussian errors δ_i. The R-package `lmvar` [33] that implements a maximum likelihood approach was used to fit the model.

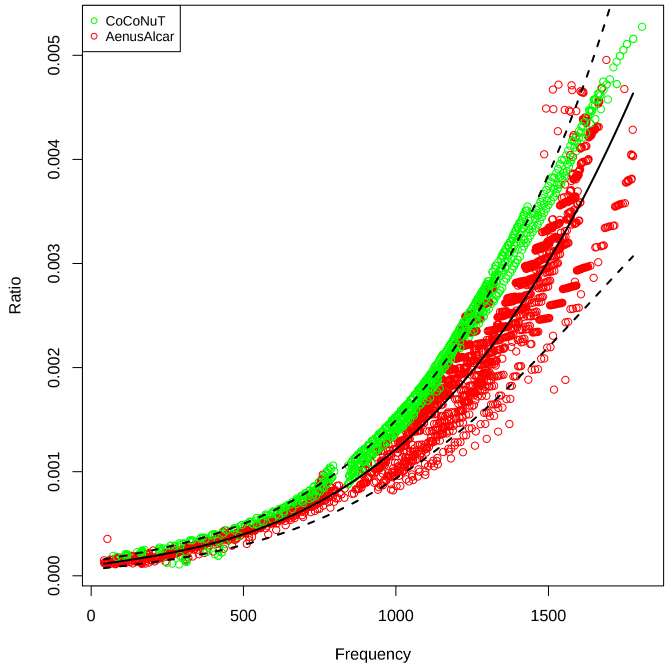

FIG. 1. Ratio $M_{\mathrm{PNS}}/R_{\mathrm{PNS}}^2$ from 25 1D simulations AENUS-ALCAR (red) and CoCoNuT (green) code. The solid line is the maximum likelihood estimate of heteroscedastic cubic model with 95% confidence bands (dashed lines) considering the AENUS-ALCAR data points.

The best fitting model amongst polynomials of degree 1, 2, and 3 was chosen according to the Aikaike information criterion with coefficients given in Table II, which is actually the model defined in (1). The data and fit of the model including 95% confidence bands are displayed in Figure 1.

Coefficient	Estimate	Standard error
β_1	1.00×10^{-06}	2.12×10^{-08}
β_2	-8.22×10^{-10}	5.00×10^{-11}
β_3	1.01×10^{-12}	2.70×10^{-14}
α_0	$-1.02 \times 10^{+01}$	6.80×10^{-02}
α_1	7.24×10^{-04}	1.56×10^{-04}
α_2	6.23×10^{-07}	8.15×10^{-08}

TABLE II. Estimate and standard error of the coefficients of the best fit model describing the ratio $r = M_{\mathrm{PNS}}/R_{\mathrm{PNS}}^2$ as function of the frequency of the ${}^2g_2$ mode.

To develop the method we considered the gravitational wave signal s20S described in Section II, originally sampled at 16384 Hz but resampled at 4096 Hz. A spectrogram of this signal is shown in Figure 2 based on autoregressive estimates of the local spectra for successive time intervals of length 200 with a 90% overlap. The dominant emission mode corresponds to the PNS oscillation ${}^2g_2$-mode. We have developed a time-frequency method to track the ridge $m(t)$ in the spectrogram, taking into account that it is monotonically increasing as time goes, a property of the ${}^2g_2$-mode. Starting from either the left- or right-most column of the time-frequency matrix we identify and trace the sequence of amplitude peaks within a certain frequency band given the monotonicity constraint. Appendix A is providing more details on the reconstruction of the g mode ridge.

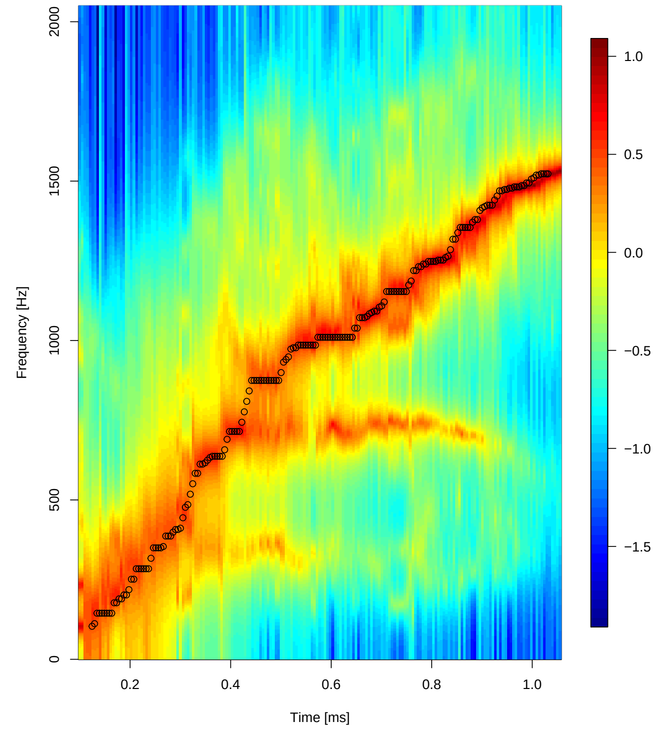

FIG. 2. Spectrogram of the gravitational wave signal s20S sampled at 4096 Hz. The spectrogram is obtained using data streach of 200 samples overlapping at 90% with each other.

We collect the instantaneous frequency $f(t_i)$ corresponding to the ridge $m(t_i)$ for the midpoint t_i of each local time interval of the spectrogram and interpolating $f(t)$ for values in between the t_i. We then use equation (1) to obtain estimates of the time evolution of the ratio together with 95% confidence intervals. An exemple is given in Figure 3 where the red points are the point estimates and the grey bands represent 95% confidence bands. Ratio values computed using the mass and radius values obtained from the simulation code are shown in black.

In this case, for a GW signal without any noise, the coverage of our 95% confidence band is 94%. In the next section we investigate the performance of reconstruction

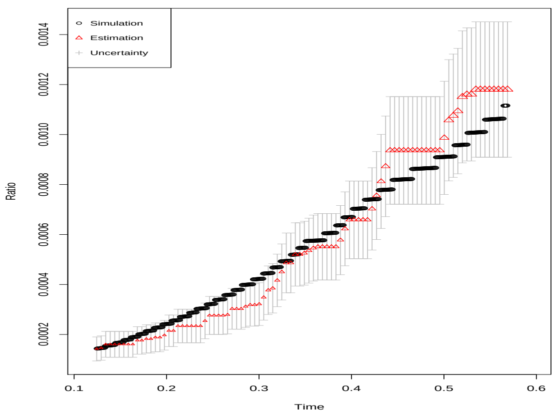

FIG. 3. Ratio $M_{\rm PNS}/R^2_{\rm PNS}$ as function of time extracted from the ${}^2g_2$-mode of the `s20S` signal (red points and the 95% confidence belt in grey) compared to the ratio value derived from the PNS mass and radius given by the simulation code (black points).

of $r(t)$ when the gravitational wave signal is embedded in noise.

IV. DETECTION SENSITIVITY WITH ADVANCED GRAVITATIONAL WAVE DETECTORS

To estimate how accurately we can infer the time evolution of $r = M_{\rm PNS}/R^2_{\rm PNS}$ in the gravitational wave detector data, we have added `s20S` GW signal to 100 Gaussian noise realisations whose power spectral density follows advanced LIGO (aLIGO) spectrum [34] shown on Figure 5. We have varied the distance to the source, covering a large range of distances for which a detection in second generation of gravitational wave detectors is feasible. The source is optimally oriented with respect to the gravitational wave detector. We are assuming a GW signal from a core collapse phenomena has been identified in the data and that the beginning of the GW signal is known within $O(10\ ms)$. The data (signal embedded in noise) are whitened using the function *prewhiten* of the R-package TSA. An auto-regressive model with maximal 100 coefficients has been used.

For each of the noise realisations, we reconstruct the ratio time series r_i of length N starting from the left side of the spectrogram and constraining the beginning of the track to be smaller than 200 Hz. The reconstructed ratio is then compare to the "true" ratio r_i^0 derived from the PNS mass and radius generated by the simulation code that produced `s20S`.

Figure 4 is showing the fraction of the ratio r_i^0 values

Simulation	`s11`	`s15`	`s15S`	`s15G`	`s20`	`s20S`	`s25`	`s40`
aLIGO char. distance (kpc)	7	26	25	21	16	11	9	12
SNR in aLIGO	19.5	55.4	59.0	60.0	34.3	35.8	116.5	98.5
CE2 char. distance (kpc)								
SNR in CE2								

TABLE III. Matched filter signal-to-noise ratio (SNR) of the simulated waveforms for the different GW detectors considered in this study. The source is located at 10 kpc and is optimally oriented with respect to the detector.

that fall within the 95% confidence interval of r_i. This quantity, *coverage*, is taking maximal values when the source is located within few kpc and then decreases with the distance.

To better quantify how well we reconstruct the ratio, we have also considered Δ the mean over the track of the relative error of r_i.

$$\Delta = \frac{1}{N}\sum_{1}^{N}\frac{|r_i - r_i^0|}{r_i^0} \tag{3}$$

Δ values of each of the 100 noise realisation are shown as well as function of the distance on Figure 4. For a source located up to ∼10 kpc the relative error remains smaller than 20%. At small distance Δ is small but not null. This reflects the approximation of the model used for r. It is nevertheless remarkable that one can reconstruct the ratio time series with a good precision at distance up to ∼ 10 kpc for this particular waveform, with *coverage* value larger than 80%. We have tested that the method does not depend on features of `s20S` using 7 other waveforms described in section II covering a large range of progenitor masses. Figure 6 shows that apart `s11.2-LS220`, the ratio is well reconstructed for all waveforms up to ∼ 10kpc. On this figure we also show the *coverage* value in case of absence of signal. The median value is significantly different from 0 because the g-mode reconstruction algorithm is looking for a continuously frequency increasing track in the spectrogram, starting between 0 and 200 Hz. In Table ?? we are reporting the distance at which *coverage* median is lower than 80%.

V. DISCUSSION

Acknowledgments —

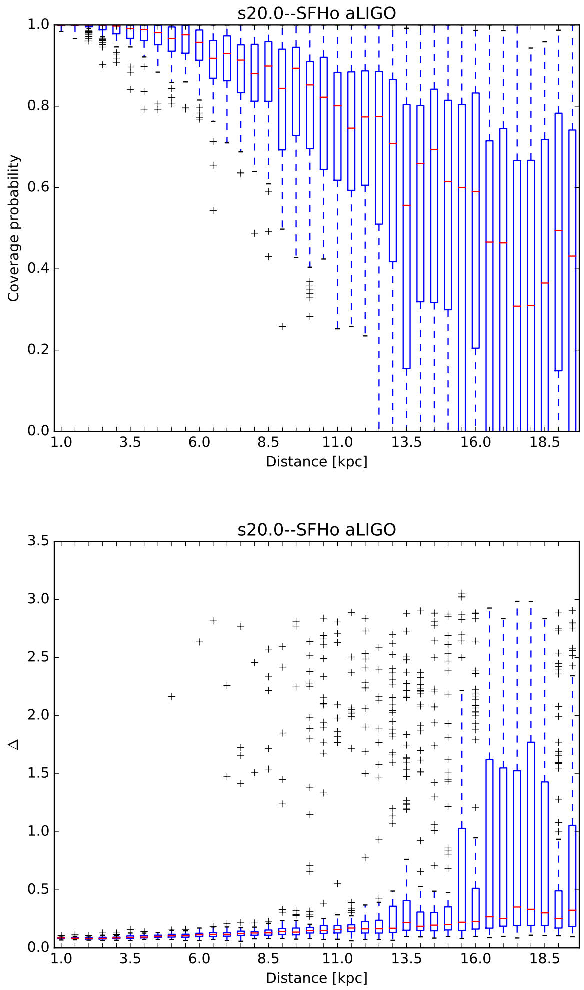

FIG. 4. Boxplots of *coverage* (upper panel) and Δ (lower panel) for s20S signal embedded in aLIGO noise at different distances from the Earth. 100 noise realisations is considered for each distance.

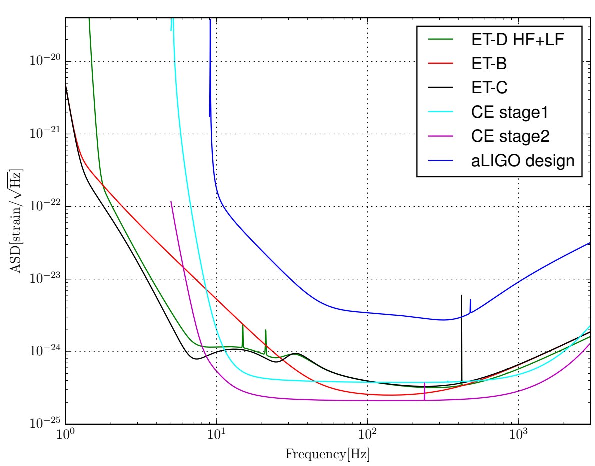

FIG. 5.

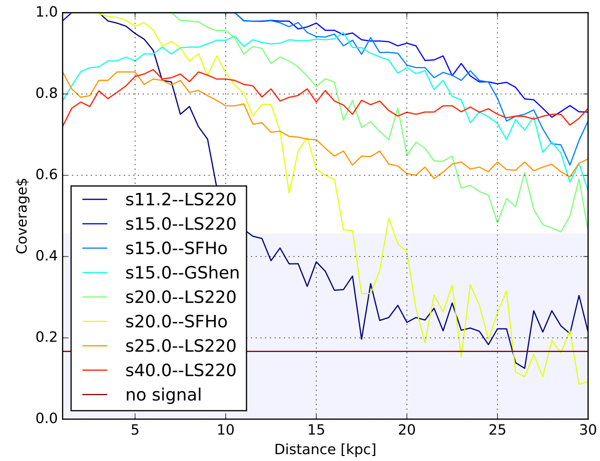

FIG. 6. Median of *coverage* for 8 CCSN waveforms embedded in aLIGO noise and located at different distance from the Earth. The "no signal" line and band show the median and first and third quartile of *coverage* in absence of any signal.

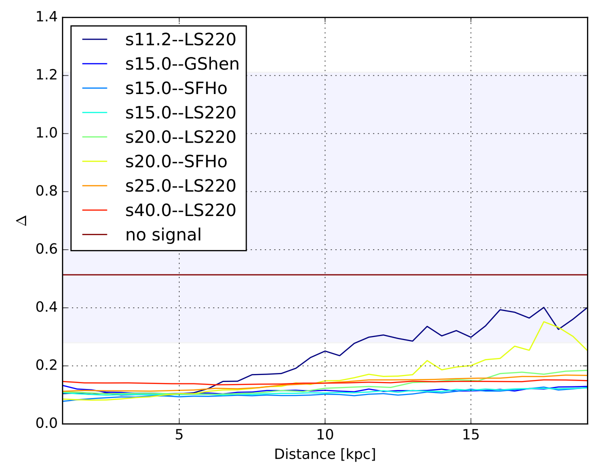

FIG. 7. Median of *Delta* for 8 CCSN waveforms embedded in aLIGO noise and located at different distance from the Earth. The "no signal" line and band show the median and first and third quartile of *Delta* in absence of any signal.

Appendix A G-MODE RECONSTRUCTION

Given the spectrogram and an specified time interval for the g-mode reconstruction, our proposal method works as follows. The starting point must be specified. It can be either at the beginning or at the end of the signal. Then, in one of these extremes, the maximum energy value is identified, registering its frequency. This is done independently for a number of consecutive time intervals. Then we calculate the median of these frequency values, providing a robust starting value for the g-mode reconstruction.

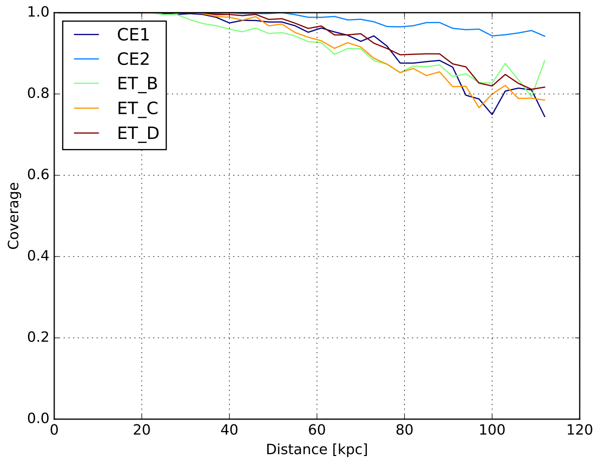

FIG. 8. Median of *coverage* for s20.0–SFHo CCSN waveform embedded in 3G detectors noise and located at different distance from the Earth.

The starting frequency value is the first g-mode estimate for the first or the last time interval, depending on the specified starting location. If the reconstruction is set to start at the beginning of the signal, the reconstruction will be done progressively over the time intervals, where each maximum frequency value will be calculated within a frequency range specified by the previous g-mode estimate. Given the non-decreasing behaviour of the true g-mode values, the g-mode estimates will be forced to be greater or equal than the one estimated for its previous time interval, and lower than a specified upper limit. As a result, the g-modes estimates will be a non-decreasing sequence of frequency values.

If the reconstruction is set to start at the end of the signal, the g-modes will be estimated backward in time. Each maximum frequency is calculated within a range determined by its successor (in time) g-mode estimate. These estimates are forced to be lower or equal than its successor (in time) estimate, but greater than a specified lower limit. Thus, a non-decreasing sequence of g-mode estimates is guaranteed.

This g-mode reconstruction method works if and only if the signal is strong enough to provide information about the g-mode, which is reflected in the spectrogram.

Given the sequence of g-mode estimates, the confidence band will be calculated by using the model defined in (**??**). The g-mode estimates are frequency values which we use as predictors in the model in order to generate confidence intervals for the ratios. Since the g-mode estimates are indexed by time, the confidence intervals for the ratios are too. Thus, we generate the confidence band by interpolating the lower and upper limits of the collection of consecutive confidence intervals, which will be valid for the time range of the g-mode estimates. This confidence band is used to estimate the coverage probabilities in our simulation studies presented below.

[1] S.E. Gossan, P. Sutton, A. Stuver, M. Zanolin, K. Gill, and C. Ott, "Observing gravitational waves from core-collapse supernovae in the advanced detector era," Physical Review D **93** (2016), 10.1103/physrevd.93.042002.

[2] C. D. Ott, H. Dimmelmeier, A. Marek, H.-T. Janka, B. Zink, I. Hawke, and E. Schnetter, "Rotating collapse of stellar iron cores in general relativity," Classical and Quantum Gravity **24**, 139–+ (2007), arXiv:astro-ph/0612638.

[3] E. Abdikamalov, S. Gossan, A. M. DeMaio, and C. D. Ott, "Measuring the angular momentum distribution in core-collapse supernova progenitors with gravitational waves," Phys. Rev. D **90**, 044001 (2014), arXiv:1311.3678 [astro-ph.SR].

[4] Sherwood Richers, Christian D. Ott, Ernazar Abdikamalov, Evan O'Connor, and Chris Sullivan, "Equation of state effects on gravitational waves from rotating core collapse," Phys. Rev. D **95**, 063019 (2017), arXiv:1701.02752 [astro-ph.HE].

[5] K.D. Kokkotas and B.G. Schmidt, "Quasi-normal modes of stars and black holes," Living Rev. Rel. **2**, 2 (1999).

[6] John L. Friedman and Nikolaos Stergioulas, *Rotating Relativistic Stars* (2013).

[7] J. W. Murphy, C. D. Ott, and A. Burrows, "A Model for Gravitational Wave Emission from Neutrino-Driven Core-Collapse Supernovae," Astrophys. J. **707**, 1173 (2009).

[8] Pablo Cerdá-Durán, Nicolas DeBrye, Miguel A. Aloy, José A. Font, and Martin Obergaulinger, "Gravitational Wave Signatures in Black Hole Forming Core Collapse," Astrophys. J. Lett. **779**, L18 (2013), arXiv:1310.8290 [astro-ph.SR].

[9] B. Müller, H.-T. Janka, and A. Marek, "A New Multi-dimensional General Relativistic Neutrino Hydrodynamics Code of Core-collapse Supernovae. III. Gravitational Wave Signals from Supernova Explosion Models," Astrophys. J. **766**, 43 (2013), arXiv:1210.6984 [astro-ph.SR].

[10] Konstantin N. Yakunin, Anthony Mezzacappa, Pedro Marronetti, Shin'ichirou Yoshida, Stephen W. Bruenn, W. Raphael Hix, Eric J. Lentz, O. E. Bronson Messer, J. Austin Harris, Eirik Endeve, John M. Blondin, and Eric J. Lingerfelt, Phys. Rev. D **92**, 084040 (2015), arXiv:1505.05824 [astro-ph.HE].

[11] Takami Kuroda, Kei Kotake, and Tomoya Takiwaki, "A New Gravitational-wave Signature from Standing Accretion Shock Instability in Supernovae," Astrophys. J. Lett. **829**, L14 (2016), arXiv:1605.09215 [astro-ph.HE].

[12] H. Andresen, B. Müller, E. Müller, and H. Th. Janka, "Gravitational wave signals from 3D neutrino hydrodynamics simulations of core-collapse supernovae," MNRAS **468**, 2032–2051 (2017), arXiv:1607.05199 [astro-ph.HE].

[13] P. N. McDermott, H. M. van Horn, and J. F. Scholl, "Nonradial g-mode oscillations of warm neutron stars," Astrophys. J. **268**, 837–848 (1983).

[14] A. Reisenegger and P. Goldreich, "A new class of g-modes in neutron stars," Astrophys. J. **395**, 240–249 (1992).

[15] V. Ferrari, L. Gualtieri, J. A. Pons, and A. Stavridis, "Gravitational waves from rotating proto-neutron stars," Classical and Quantum Gravity **21**, S515–S519 (2004), astro-ph/0409578.

[16] A. Passamonti, M. Bruni, L. Gualtieri, and C. F. Sopuerta, "Coupling of radial and nonradial oscillations of relativistic stars: Gauge-invariant formalism," Phys. Rev. D **71**, 024022 (2005), gr-qc/0407108.

[17] H. Dimmelmeier, N. Stergioulas, and J. A. Font, "Non-linear axisymmetric pulsations of rotating relativistic stars in the conformal flatness approximation," MNRAS **368**, 1609–1630 (2006), astro-ph/0511394.

[18] C. J. Krüger, W. C. G. Ho, and N. Andersson, "Seismology of adolescent neutron stars: Accounting for thermal effects and crust elasticity," Phys. Rev. D **92**, 063009 (2015), arXiv:1402.5656 [gr-qc].

[19] G. Camelio, A. Lovato, L. Gualtieri, O. Benhar, J. A. Pons, and V. Ferrari, "Evolution of a proto-neutron star with a nuclear many-body equation of state: neutrino luminosity and gravitational wave frequencies," ArXiv e-prints (2017), arXiv:1704.01923 [astro-ph.HE].

[20] H. Sotani and T. Takiwaki, "Gravitational wave asteroseismology with protoneutron stars," Phys. Rev. D **94**, 044043 (2016), arXiv:1608.01048 [astro-ph.HE].

[21] A. Torres-Forné, P. Cerdá-Durán, A. Passamonti, and J. A. Font, "Towards asteroseismology of core-collapse supernovae with gravitational-wave observations - I. Cowling approximation," MNRAS **474**, 5272–5286 (2018), arXiv:1708.01920 [astro-ph.SR].

[22] A. Torres-Forné, P. Cerdá-Durán, A. Passamonti, M. Obergaulinger, and J. A. Font, "Towards asteroseismology of core-collapse supernovae with gravitational wave observations - II. Inclusion of space-time perturbations," MNRAS **482**, 3967–3988 (2019), arXiv:1806.11366 [astro-ph.HE].

[23] A. Torres-Forné, P. Cerdá-Durán, M. Obergaulinger, B. Müller, and J. Font, "Universal relations for gravitational-wave asteroseismology of proto-neutron stars," Physical Review Letters **123**, 051102 (2019).

[24] O. Just, M. Obergaulinger, and H.-T. Janka, "A new multidimensional, energy-dependent two-moment transport code for neutrino-hydrodynamics," MNRAS **453**, 3386–3413 (2015), arXiv:1501.02999.

[25] P. Cerdá-Durán, J. A. Font, L. Antón, and E. Müller, "A new general relativistic magnetohydrodynamics code for dynamical spacetimes," A&A **492**, 937–953 (2008), arXiv:0804.4572.

[26] B. Müller and H. Th. Janka, "Non-radial instabilities and progenitor asphericities in core-collapse supernovae," MNRAS **448**, 2141–2174 (2015), arXiv:1409.4783 [astro-ph.SR].

[27] A. Marek, H. Dimmelmeier, H.-T. Janka, E. Müller, and R. Buras, "Exploring the relativistic regime with Newtonian hydrodynamics: an improved effective gravitational potential for supernova simulations," A&A **445**, 273–289 (2006).

[28] S. E. Woosley, A. Heger, and T. A. Weaver, "The evolution and explosion of massive stars," Reviews of Modern Physics **74**, 1015–1071 (2002).

[29] J. M. Lattimer and F. Douglas Swesty, "A generalized equation of state for hot, dense matter," Nuclear Physics A **535**, 331–376 (1991).

[30] A. W. Steiner, M. Hempel, and T. Fischer, "Core-collapse Supernova Equations of State Based on Neutron Star Observations," Astrophys. J. **774**, 17 (2013), arXiv:1207.2184 [astro-ph.SR].

[31] G. Shen, C. J. Horowitz, and S. Teige, "New equation of state for astrophysical simulations," Phys. Rev. C **83**, 035802 (2011), arXiv:1101.3715 [astro-ph.SR].

[32] S. E. Woosley and A. Heger, "Nucleosynthesis and remnants in massive stars of solar metallicity," Phys. Rep. **442**, 269–283 (2007), astro-ph/0702176.

[33] .

[34] Lisa Barsotti, Peter Fritschel, Matthew Evans, and Slawomir Gras, "Updated advanced ligo sensitivity design curve," (2018).